Communication

Designing Advanced Multistatic Imaging Systems with Optimal 2D Sparse Arrays

Lorena Perez-Eijo [1,*] ![ORCID], **Marcos Arias** [1] ![ORCID], **Borja Gonzalez-Valdes** [1] ![ORCID], **Yolanda Rodriguez-Vaqueiro** [1] ![ORCID],
Oscar Rubiños [1] ![ORCID], **Antonio Pino** [1] ![ORCID], **Ignacio Sardinero-Meirás** [2] ![ORCID] and **Jesús Grajal** [2] ![ORCID]

1   AtlanTTic Research Center, Universidade de Vigo, 36310 Vigo, Spain
2   Information Processing and Telecommunications Center, Universidad Politecnica de Madrid,
     28040 Madrid, Spain
*   Correspondence: lorena@com.uvigo.es

Abstract: This study introduces an innovative optimization method to identify the optimal configuration of a sparse symmetric 2D array for applications in security, particularly multistatic imaging. Utilizing genetic algorithms (GAs) in a sophisticated optimization process, the research focuses on achieving the most favorable antenna distribution while mitigating the common issue of secondary lobes in sparse arrays. The main objective is to determine the ideal configuration from specific design parameters, including hardware specifications such as number of radiating elements, minimum spacing, operating frequency range, and image separation distance. The study employed a cost function based on the the point spread function (PSF), the system response to a point source, with the goal of minimizing the secondary lobe levels and maximizing their separation from the main lobe. Advanced simulation algorithms based on physical optics (PO) were used to validate the presented methodology and results.

Keywords: submillimeter wavelength imaging; multistatic imaging; backpropagation imaging; genetic algorithm (GA)

1. Introduction

Active millimeter- and submillimeter-wave radar systems have become indispensable tools for bolstering civil security in airports, bus stations, crowded public areas, and beyond [1–7]. These non-destructive testing (NDT) systems play a pivotal role in security screening by detecting concealed objects, including weapons and drugs, providing effective and secure solutions.

Conventional monostatic and quasi-monostatic radar systems [8–11] face limitations in complex geometries due to shadow regions caused by specular reflections falling outside the receiving area. To overcome this limitation, our proposal integrates multiple wideband millimeter-wave transmitters and receivers to obtain high-resolution radar images in real-time [12–15]. Multistatic systems provide several advantages by capturing information from multiple angles, including advanced stealth object detection and reduced susceptibility to jamming. In addition, this approach allows for a lower spatial sampling frequency than traditional systems, which benefits from secondary lobe cancellation [16–19]. Unlike other commonly used methods for image processing, such as fractal wavelets [20–26], the approach of this study extracts artifacts by averaging the phasors of the electromagnetic fields acquired by the multistatic system.

In this paper, we present a novel methodology for identifying an optimal 2D sparse array configuration for generating multistatic radar images based on predefined design parameters. While various array configurations exist for THz security applications, we chose a uniform sparse array configuration due to its suitability for our research problem. Conventional dense arrays offer superior image resolution but require a significant number

of elements, resulting in unwieldy arrays, high computational requirements, and potential impracticality for real-time applications. In contrast, random distributions offer a simpler design process and the potential for improved resolution compared to uniform meshes but lack the systematic performance optimization characteristic of our chosen methodology and occasionally yield unpredictable image quality [27].

Genetic algorithms (GAs) have emerged as the preferred method for array optimization due to their adaptability, robustness, and efficiency in tackling complex array design problems encountered in scientific research. GAs excel at exploring large search spaces; handling non-linear, non-convex optimization landscapes; and supporting multi-objective optimization. They are highly efficient in combinatorial search spaces and work effectively with black-box functions, making them suitable for complex optimization challenges.

The core objective of this study is to identify the optimal antenna configuration from a set of design parameters. The structure of this paper unfolds as follows: Section 2 outlines the architecture, imaging procedure, and the evaluation function used for potential solutions. In Section 3, we introduce GAs and describe their specific application in this context. Section 4 delves into the simulation process, while Section 5 presents the results, including a compelling comparison between optimized and non-optimized approaches. Finally, in Section 6, we summarize our achievements and lay out future steps to further enhance imaging system efficiency.

2. Multistatic Architecture

A multistatic architecture refers to a configuration in which multiple spatially distributed transmitters and receivers collaborate to perform sensing or imaging tasks. This architecture contrasts with traditional monostatic radar systems, where a single radar unit serves as both the transmitter and the receiver.

In a multistatic radar system, each transmitter emits electromagnetic waves toward the designated area of interest. Multiple receivers are strategically placed in various locations to simultaneously detect reflections or echoes of waves that were transmitted and interacted with targets in the surrounding environment.

The main idea behind multistatic architectures is to utilize the spatial diversity of receivers to obtain more detailed and comprehensive information regarding the observed scene. These approaches offer several advantages in both scientific and practical applications, including:

- Multistatic architectures can achieve increased spatial resolution through the collection of data from various angles. This provides the system with the ability to distinguish small details, resulting in more precise measurements that are paramount in the identification of targets, object recognition, and other imaging tasks.
- Deploying transmitters and receivers across multiple locations improves system resilience, making it harder for adversaries to disrupt. In case one component is compromised, the system remains operational with the unaffected ones.
- Multistatic systems reduce blind spots caused by obstructions or interference, achieved through the use of multiple sensors, which provide comprehensive coverage.
- Multistatic radar systems are highly effective in detecting and tracking stealth targets that exhibit low visibility due to their inability to maintain stealth from all angles, thus becoming more visible from diverse viewpoints.
- The designs of multistatic systems are flexible and allow for customized configurations that meet specific operational requirements, accommodating a wide range of applications.

These advantages collectively make multistatic radar systems a valuable tool for defense and surveillance applications.

These systems are primarily designed for real-time personal security and surveillance applications. Therefore, it is vital to minimize the number of elements needed, which can be achieved by opting for sparse arrays instead of the denser ones that are generally used. Sparse arrays offer many advantages in this context. In particular, they improve cost

efficiency by reducing the number of antenna elements required, leading to savings in hardware acquisition, deployment, and maintenance. They also reduce the computational load for signal processing and data analysis, which is critical for real-time applications. These arrays demonstrate versatility by seamlessly adapting to different scenarios and skillfully balancing performance and complexity. Most importantly, they address resource conservation and environmental sustainability by requiring fewer resources. Using sparse arrays strategically optimizes performance while efficiently managing resources and complexity compared to denser alternatives.

2.1. Baseline Configuration

This work marks the initial phase in the development of a prototype, which is currently undergoing construction. As a result, design constraints have been defined by considering the available hardware and its specific characteristics. The system's architecture relies on multiple transmitters (tx_m) and receivers (rx_n), positioned at t_m and r_n, respectively. This work focuses on analyzing a specific architecture consisting of a 2D sparse array with 64 transmitting antennas (NTX) and 49 receiving antennas (NRX) positioned in front of an object under test (OUT).

The transmitting antennas are equidistantly spaced at a distance of d_{tx} cm, while the receiving antennas are also equidistantly spaced at a distance of d_{rx}. To ensure symmetrical responses with respect to both the X = 0 and Z = 0 axes, this equidistance is maintained in both the horizontal and vertical directions. The system operates in the frequency range of 120 to 150 GHz using only 12 different frequencies, which corresponds to a minimum working wavelength (λ_{min}) of 2 mm.

2.2. Imaging

The imaging process involves creating an individual image for each transmitting antenna, combining contributions from all receivers to create the final image. Figure 1 provides a visual representation, simplifying the procedure within a basic system configuration of NTX = 3 and NRX = 2.
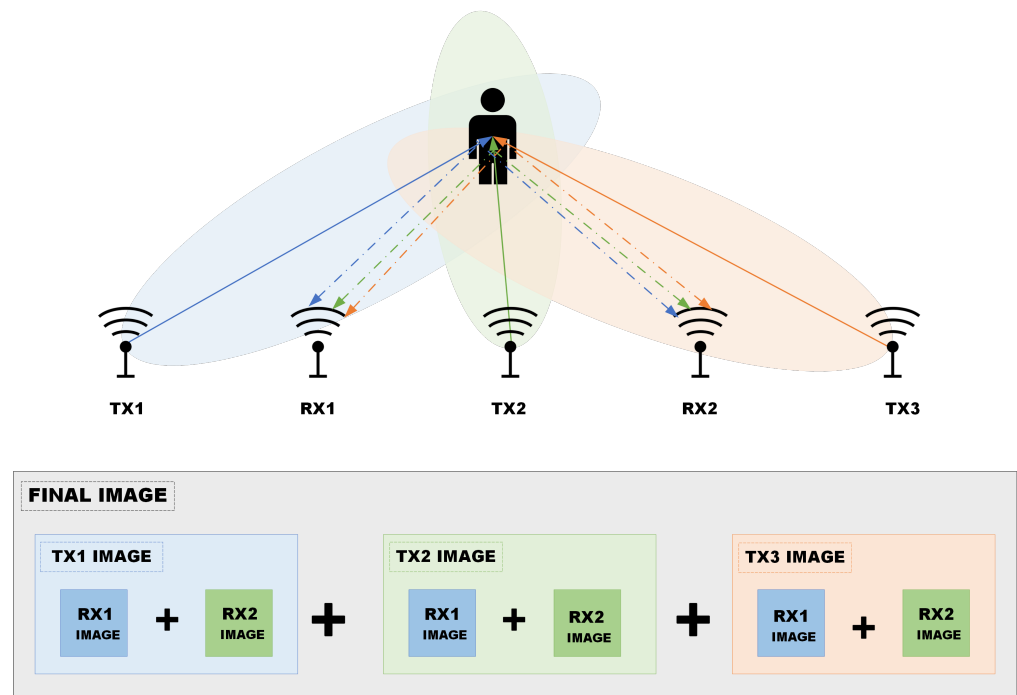

Figure 1. Graph of the imaging process in a simplified system with NTX = 3 and NRX = 2.

In this concept, each transmitting antenna emits signals toward the OUT, creating distinct electromagnetic responses from the target. Receiving antennas systematically

capture these responses, reflecting the unique interaction of the transmitted signals with the object. Coherent summation of these responses, encompassing phase and amplitude information, is performed for each transmitting antenna.

As a result, for a system with NTX transmitting antennas, NTX transmitter images are generated, each representing a unique perspective offered by a specific transmitting element.

The final image is created by combining these transmitter images coherently. It provides a comprehensive depiction of the object under scrutiny, revealing intricate characteristics and spatial distribution. This fusion of information from multiple transmitting antennas enhances imaging resolution and fidelity, offering a more detailed and accurate representation of the target object.

2.3. Point Spread Function

The PSF plays a crucial role in radar systems, as it defines how electromagnetic waves interact with point-like targets, guiding the detection and localization of objects. It characterizes the spatial distribution of radar energy received from a point scatterer and directly impacts the system's resolution. A smaller PSF signifies higher radar resolution, enabling the distinction of closely spaced targets. Various factors, including radar frequency, antenna characteristics, and signal processing methods, influence the PSF, thereby affecting the accuracy of target localization. Thus, a comprehensive understanding of the PSF is indispensable for optimizing radar systems utilized in surveillance, tracking, and remote sensing applications.

According to the reciprocity theorem, the total PSF of the system when focused at point p_i can be computed from the PSF of the transmitting and receiving arrays as follows [28]:

$$PSF_{tx}(p_i) = \sum_{l,m} e^{-j\kappa_l |t_m - p_i|} \tag{1}$$

$$PSF_{rx}(p_i) = \sum_{l,n} e^{-j\kappa_l |r_n - p_i|} \tag{2}$$

$$PSF_{total}(p_i) = PSF_{tx}(p_i) \times PSF_{rx}(p_i) \tag{3}$$

Here, multiple frequencies f_l are employed in an ultra wideband (UWB) radar configuration, and $\kappa_l = 2\pi \frac{f_l}{c}$ represents the wavenumber at the l-th frequency.

3. Optimization Algorithm

In the realm of mathematical and computational sciences, the choice between using optimization algorithms and exhaustively exploring all feasible solutions depends on a reasonable trade-off between efficiency, scalability, and accuracy. When faced with complex optimization challenges characterized by a large solution space, the use of optimization algorithms is a methodologically sound choice. The effectiveness of optimization algorithms is further manifested in their ability to handle constraints and ensure the precise attainment of predefined objectives, thereby providing solutions that satisfy the desired criteria. In addition, their adaptability allows the tailoring of optimization strategies to different types of problems, increasing their utility in academic and scientific domains. Consequently, optimization algorithms represent a rational preference for cases that require computational rigor and scalability, making them indispensable in scenarios where comprehensive exploration of all solution alternatives is infeasible or prohibitively resource-intensive.

3.1. Cost Function

In optimization, the cost function plays a vital role in evaluating solution efficiency and appropriateness within the problem space. Its primary objective is to measure solution quality in terms of optimization objectives while considering problem constraints to enable numerical performance evaluation. The optimization algorithm aims to minimize a function to identify the ideal solution among multiple options. In this case, the goal is to establish

the transmitter element spacing (d_{tx}) and receiver element spacing (d_{rx}) combination that yields the lowest magnitude of the secondary lobes.

Figure 2 shows the cost function for the case under study. As expected, it presents complex, non-linear, discontinuous, and non-convex landscapes. Furthermore, not every value fulfills the problem requirements, resulting in a difficult optimization task. Therefore, we utilized the GA optimization algorithm due to its ability to handle such complexity. The next sections provide the rationale for selecting this technique over others and the details of the implementation for this particular issue.
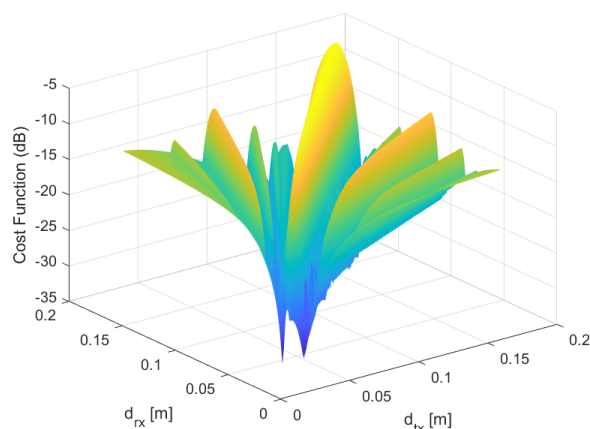

Figure 2. Cost function associated with each possible combination of $d_{tx} - d_{rx}$.

3.2. Genetic Algorithm

The cost function utilized in this method (as demonstrated in Section 3.1) creates landscapes that tend to be complex, nonlinear, often non-convex, and (more importantly) not continuous, posing formidable challenges for optimization.

Gradient methods, Bayesian optimization, simulated annealing, or and colony optimization techniques [29–36] are well-known methods that work well in scenarios with smooth and well-behaved objective functions.

In contrast, GAs present a compelling set of characteristics that make them the ideal choice for this problem. Their ability to navigate high-dimensional solution spaces, coupled with their resilience in dealing with noisy or irregularly sampled objective functions, positions them as a robust and versatile optimization tool. The adaptive nature of GAs, which merge the best solutions and introduce mutations, facilitates extensive exploration of the solution space, greatly increasing the likelihood of finding globally optimal configurations. In addition, GAs are amenable to parallelization, leveraging the computational power of modern resources to accelerate the optimization process.

GAs have demonstrated remarkable efficacy in tackling real-world challenges [37–40]. They operate within a population-based framework, where each member represents a potential solution. The fitness of individuals gauges their problem-solving capabilities. Highly fit individuals reproduce by mating with others, passing on their advantageous traits. This orchestrated progression births a new generation with the promise of enhanced solutions.

GAs conduct this evolutionary process by combining genetic material from the most promising individuals through recombination (crossover) and introducing occasional mutations. As generations unfold, GAs tend toward optimization. Top-performing individuals propagate favorable traits and information, while mutations prevent stagnation. Consequently, GAs adeptly navigate complex search spaces, as depicted in Figure 3.

A well-designed GA can converge on optimal solutions, offering strength in diverse problem domains. Although GAs cannot guarantee global optimality due to inherent randomness, they often quickly find practical solutions that suffice for real-world applications.
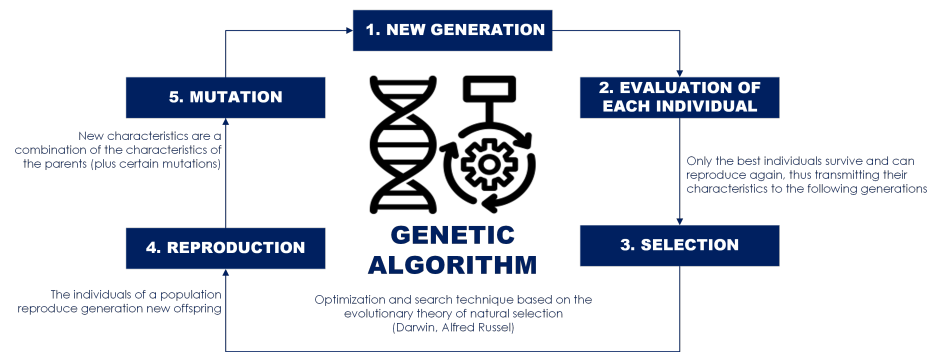
Figure 3. Basic GA operation.

3.2.1. Custom GA Configuration

Once the optimization tool has been selected, the optimal configuration with the smallest secondary lobes should be identified. Only configurations that meet the criteria below will be evaluated:

- The aperture size (horizontal and vertical) cannot exceed 100 cm.
- Due to hardware limitations, the minimum distance between elements is set to 2 cm.
- The array is symmetric on both the X and Z axes.
- Transmitter and receiver elements are uniformly spaced in both horizontal and vertical dimensions.

In this study, the GA was utilized to calculate the most suitable d_{rx} value, while d_{tx} was kept constant. Although there were previous attempts to optimize both variables at the same time, it was found that fixing the value of d_{tx} to cover the desired aperture size and concentrating on determining the optimal d_{rx} value is a more efficient method.

This process is computationally intensive, as the GA solver must construct the appropriate architecture, compute the PSF, and evaluate the cost function for each potential d_{tx}-d_{rx} pair. However, by taking advantage of GPU acceleration and MATLAB's vector computation capabilities, we can quickly and efficiently obtain initial results. Fixing d_{tx} while optimizing only for d_{rx} yields results in less than 3 min and 18 s. If both d_{tx} and d_{rx} are optimized simultaneously, the process extends to about 15 min.

3.2.2. MATLAB Implementation

Optimization was performed using MATLAB's GA Toolbox, which provides a platform for creating and using GAs. The function *ga* requires a series of input parameters to adapt the optimization problem. The most important inputs are described below:

1. **Cost Function** (CostFcn): This parameter represents the function that needs to be optimized. It takes a set of input decision variables and generates a single value, the cost, to be minimized. As previously noted, the PSF is the cost function. It receives d_{rx} as an input and produces the PSF value related to the array configuration obtained from the combination of d_{tx}-d_{rx}.
2. **Number of decision variables** (nvars): This parameter indicates the number of variables being optimized.
3. **Linear inequality constraints** (A and b): These constraints do not apply in our situation as the problem's intrinsic characteristics depend on nonlinear constraints.
4. **Linear equality constraints** (Aeq and beq): Similarly not applicable due to the use of nonlinear constraints.
5. **Lower and upper bounds for decision variables** (lb and ub): These arrays establish the boundaries of the search space by defining the range within which each variable is permitted to vary.
6. **Initial population** (x_0): This is the initial set of candidate solutions. A randomized starting point is chosen from the feasible variable values.

7. **Options**: This structure contains a range of control settings for the behavior of the GA. It includes definitions for parameters such as population size, number of generations, genetic operators (parent selection, recombination, and mutation), and replacement strategy.

8. **Nonlinear inequality constraints** (nonlcon): An ad hoc function has been created to manage the constraints outlined in Section 3.2.1.

Once the parameters have been configured, the GA is executed, and upon completion the algorithm generates two crucial pieces of information:

*   **x** represents the optimized solution and contains the decision variables.
*   **fval** indicates the minimum value of the cost function.

4. Simulation

A simulator based on PO principles is used to model the presented system [41]. This simulator allows a comprehensive simulation of the electromagnetic response of the imaging system when exposed to an arbitrary OUT. In a first step, the simulator calculates the induced electric currents within the OUT by considering the interaction between the incident electromagnetic wave and the specific material properties and geometric characteristics of the OUT. This complex calculation is based on the solution of Maxwell's equations, which allows the derivation of the spatial distribution of the induced currents on the surface of the OUT. The simulator then determines the electromagnetic field received by each individual receiver, resulting from the field scattered by the OUT. This step is performed independently for each transmitting antenna and over a range of discrete frequencies (f_l).

In the context of radiation modeling, both the transmitting and receiving antennas are abstracted as ideal spherical sources. The OUTs are introduced into the simulator as computer-aided design (CAD) models, encapsulating their complex geometries. The detailed operation of the simulator is defined in [41]; however, for a simplified scenario involving a single tx_m, one OUT, and one rx_n, the process can be summarized as follows:

1. **Incident field calculation:** The process begins with a point source (tx_m) emitting spherical electromagnetic waves, which propagate uniformly in all directions. These waves consist of electric ($\vec{E}_{inc}$) and magnetic ($\vec{H}_{inc}$) fields traveling at the speed of light. To determine the direction of incidence, the Poynting vector ($\hat{p}_{inc}$) is calculated using the following equation:

$$\hat{p}_{inc} = Re\left\{ \frac{\vec{E}_{inc} \times \vec{H}_{inc}^*}{\|\vec{E}_{inc} \times \vec{H}_{inc}^*\|} \right\} \quad (4)$$

2. **Equivalent currents calculation:** The next step involves calculating the equivalent currents on the surface of the metallic OUT, represented as $\vec{J}_{out}$, which is responsible for radiating fields. These currents are determined as follows:

$$\vec{J}_{out} = 2\hat{n}_{out} \times \vec{H}_{inc} \quad (5)$$

3. **Scattered field calculation:** The simulator models the OUT as a collection of triangular patches with specific points and vectors, allowing for the calculation of the scattered magnetic field ($\vec{H}_{outn}$) at the receiver (rx_n) point using PO nearfield equations. This involves several substeps:

    (a) Calculate the position vector ($\vec{R}_{outn}$) between the receiver and the center of each triangular patch, along with the distance (R_{outn}) and direction ($\hat{R}_{outn}$).

    (b) Compute the magnetic field ($\vec{H}_{outn}$) at the receiver due to each triangular patch using the formula:

$$\vec{H}_{outn} = \frac{e^{-jkR_{outn}}}{4\pi R_{outn}^3}(1 + jkR_{outn})\left(\vec{J}_{out} \times \vec{R}_{outn}\right)I_{outn} \quad (6)$$

(c)   Calculate the integral term (I_{outn}) using the given expression and constants:

$$I_{outn} = 2A_{out}e^{-j\frac{\alpha_{outn}+\beta_{outn}}{3}}\left[\frac{\alpha_{outn}e^{j\beta_{outn}} - \beta_{outn}e^{j\alpha_{outn}} + \beta_{outn} - \alpha_{outn}}{(\alpha_{outn} - \beta_{outn})\alpha_{outn}\beta_{outn}}\right] \tag{7}$$

where

$$\alpha_{outn} = k\vec{v}_{out_{12}} \cdot \left(\hat{R}_{outn} - \hat{p}_{i_{out}}\right) \tag{8}$$

$$\beta_{outn} = k\vec{v}_{out_{13}} \cdot \left(\hat{R}_{outn} - \hat{p}_{i_{out}}\right) \tag{9}$$

(d)   Compute the electric field ($\vec{E}_{outn}$) at the receiver due to each triangular patch using the formula:

$$\begin{aligned}\vec{E}_{outn} = &-\frac{j\eta e^{-jkR_{outn}}}{4\pi kR_{outn}^3}\left[\vec{J}_m\left(-1 - jkR_{outn} + (kR_{outn})^2\right)\right.\\ &\left.+ \hat{R}_{outn}\left(3 + 3jkR_{outn} - (kR_{outn})^2\right)\left(\hat{R}_{outn} \cdot \vec{J}_m\right)\right]I_{outn}\end{aligned} \tag{10}$$

(e)   Simplify Equations (6) and (10), since the distance between elements is much larger than the wavelength:

$$\vec{H}_{outn} = \frac{j}{2\lambda}\frac{e^{-jkR_{outn}}}{R_{outn}}\left(\vec{J}_{out} \times \hat{R}_{outn}\right)I_{outn} \tag{11}$$

$$\vec{E}_{outn} = \eta\vec{H}_{outn} \times \hat{R}_{outn} \tag{12}$$

This entire process is iterated for all tx_m–rx_n combinations and across all f_l. Consequently, at the end of this procedure, a matrix (S_{12}) is generated, representing the received electromagnetic fields at each frequency, as observed by the receivers for each specific tx_m–rx_n pair.

This simulation was carried out so that the process was the same as that by which the measurement system was configured, with which the same (S_{12}) parameters are obtained.

In the context of ISAR (inverse synthetic aperture radar) processing on the dataset [42,43], the initial step involves defining the imaging plane of interest, which usually, but not necessarily, includes the OUT. For every tx_m–rx_n combination, two crucial distances are computed, the distance from tx_m to every point in the imaging plane (R_{inc_m}) and the distance from every point in the imaging plane to rx_n (R_{scat_n}). Once these distances are established, they are used to calculate the value of the reflected signal ($I_{(m,n)}$) as follows:

$$I_{(m,n)} = \sum_l (R_{inc_{(m)}} \cdot R_{scat_{(n)}} \cdot e^{j\kappa_l(R_{inc_{(m)}} + R_{scat_{(n)}})} \cdot S_{12_{(m,n)_{(l)}}}) \tag{13}$$

The global image (I_r) is generated by coherently adding up the individual reflected signals obtained from all tx_m–rx_n combinations. Mathematically, this summation process is represented as follows:

$$I_r = \sum_{m,n} I_{(m,n)} \tag{14}$$

I_r is a composite image that consolidates the information from all the tx_m–rx_n pairs and provides a comprehensive view of the object's scattering characteristics within the imaging plane. This global image is a valuable output of the ISAR processing, aiding in the detailed analysis and interpretation of the object's characteristics and behavior in response to electromagnetic waves.

5. Results

The results presented were obtained using the hardware described below:

- HW-1: Laptop

- 12th Gen Intel® Core™ i7-12700H @ 2.70 GHz
  * RAM: 32 GB
  * Number of Cores: 14 (20 logical cores per physical)
- 1 × NVIDIA GeForce RTX 3070 Ti Laptop GPU
  * Memory: 8 GB (GDDR6 SDRAM)
  * Number of CUDA Cores: 5888
- HW-2: Server GPU
  - 32 × 13th Gen Intel® Core™ i9-13900K @ 5.80 GHz
    * RAM: 128 GB
    * Number of Cores: 24 (32 logical cores per physical)
  - 1 × NVIDIA GeForce RTX 4090
    * Memory: 24 GB (GDDR6X)
    * Number of CUDA Cores: 16384

5.1. Optimal 2D Sparse Array

To evaluate the performance of the method, an architecture with NTX = 64 and NRX = 49 was used. As previously described in Section 3.2.1, the desired aperture size, both in range and cross-range, was set to 1 m. To precisely meet this design criterion, d_{tx} was set to 14.3 cm. Additionally, it is critical to consider the minimum inter-element separation, which was set to 2 cm due to the physical characteristics of the hardware available for prototype construction. As described in Section 2.1, the system was operated in a frequency range from 120 GHz to 150 GHz, implying the use of wavelengths in the order of 2 mm.

Given all of these design considerations, the GA was used to determine the optimal d_{rx}. Figure 4a visually depicts the progression of d_{rx} values during optimization, alongside their associated costs, until the optimal value was achieved. It is noteworthy that this graph illustrates the correlation between distance and cost, with GA convergence manifesting at the point where the distance equates to the minimal cost. The optimization process ultimately yielded an optimal value of d_{rx} = 10.0103 cm, which was subsequently employed in the construction of the optimal configuration (as shown in Figure 4b).
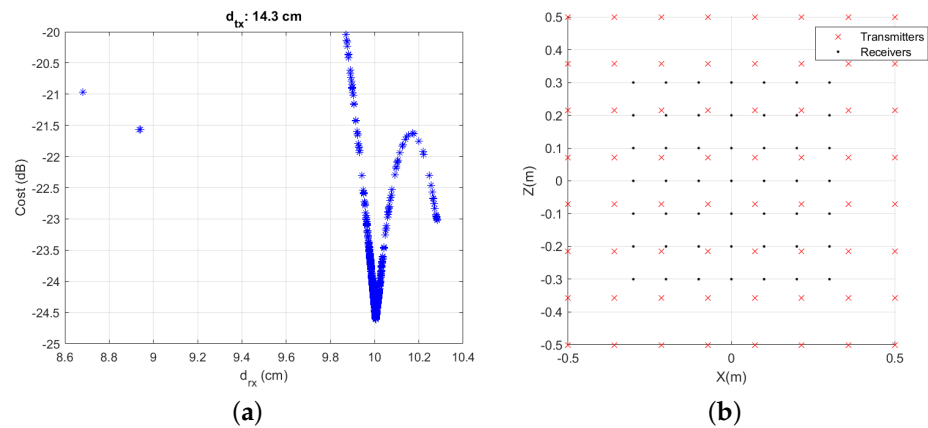

(**a**) (**b**)

Figure 4. Optimal 2D sparse array architecture via GA ($\frac{d_{rx}}{d_{tx}} = 0.6996 \approx 0.7$). (**a**) Values taken by d_{rx} during optimization and associated costs. GA convergence at 10.0103 cm. (**b**) Optimized architecture.

5.1.1. PSF

The ideal cross-range size of the PSF for this system, as described by the equation

$$\delta_{x,z} = \frac{\lambda}{D_{x,z}} \cdot L \tag{15}$$

can be understood as the spatial resolution of the imaging system [44]. In this equation, $D_{x,z}$ represents the aperture size of the array, λ represents the wavelength of the electromagnetic waves being used, and L is the distance between the OUT and the array.

The PSF effectively defines the smallest resolvable detail or spot size in the resulting images produced by the system. According to the given equation, this PSF results in a spot with an approximate diameter of 6 mm centered at the origin (0,0). This means that, in ideal conditions, the imaging system can resolve features in the object as small as this 6 mm spot size, allowing for detailed observation and analysis of the OUT's characteristics.

It is also desirable to eliminate additional contributions and minimize the presence of secondary lobes, which can have several negative effects, such as degradation of resolution, contamination of the image with unwanted artifacts, and difficulty in accurate interpretation of the image, which in turn can hinder the identification of specific objects or details. However, due to the inherent characteristics of these architectures, which do not strictly adhere to the Nyquist criterion, achieving this is unattainable. These diffraction lobes will inevitably appear as a direct consequence of the architectural features and impose constraints on the FoV during the reconstruction process. The objective is to position them as far away as possible from the main lobe and minimize their magnitude.

Secondary lobes are observed at a distance of approximately 13 cm from the main lobe and have a magnitude of 24.6 dB less than the main lobe. Although the PSF is not ideal, it comes quite close. The secondary lobes are distant enough and at a low enough level to not negatively impact the reconstructions that the system can perform.

Figure 5 shows the PSF at a distance of 3 m of the architecture resulting from the GA optimization.

The goal of the optimization is to obtain a PSF that is as clean as possible, with the aim of keeping the secondary lobes as far away and as low as possible. Without the assistance of these optimization tools, the most intuitive way to design the architecture would be to evenly distribute the transmitters and receivers along the X and Z axes. For example, to achieve a 1 m aperture, the spacing between elements should be 13.33 cm. Figure 6a shows the resulting configuration, and Figure 6b shows the PSF at 3 m. Multiple secondary lobes are observed, located extremely close to the main lobe, and furthermore, they have a significantly high level, nearly of the same order of magnitude as the main lobe. This is an unfavorable result as it predicts a significant degradation in the quality of the recovered images, making it difficult to clearly distinguish any objects. Comparing Figures 5a and 6b, there is a significant improvement of the optimized system with respect to the unoptimized one.
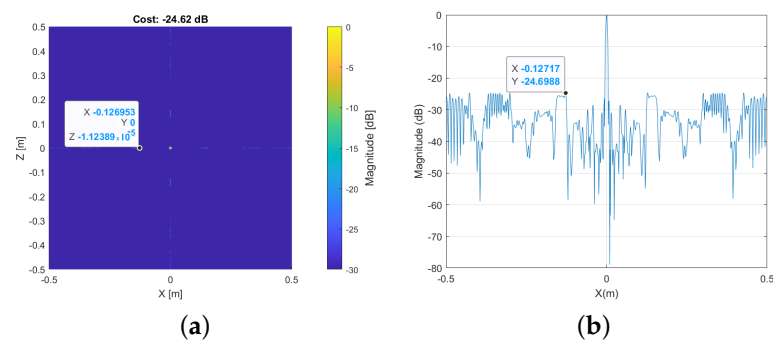

(a) (b)

Figure 5. PSF of optimal architecture at a standoff distance of 3 m. (**a**) PSF in XZ−plane. (**b**) X−Cut at Z = 0.
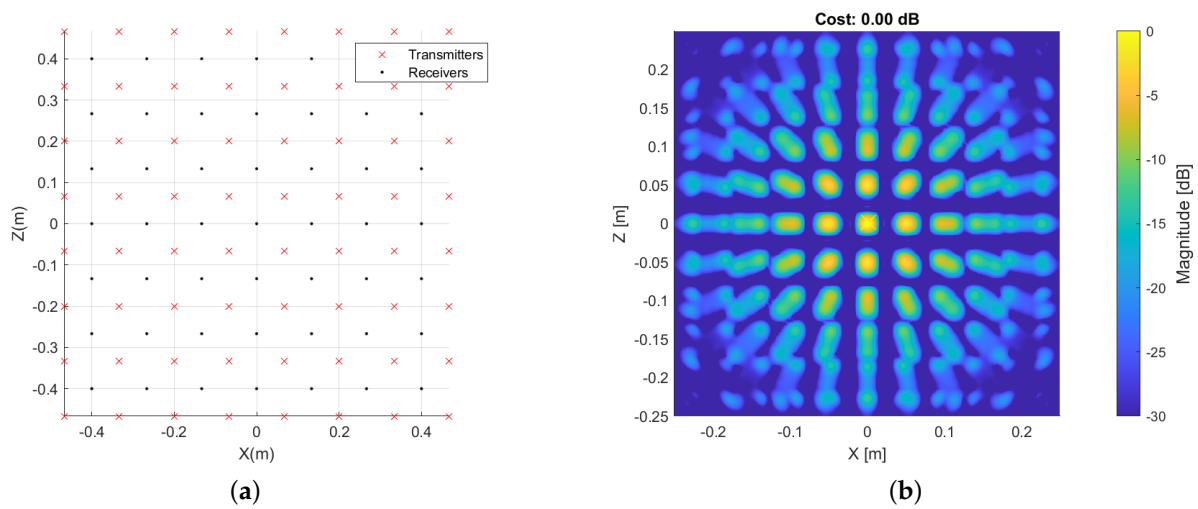
Figure 6. Non-optimized array configuration and its corresponding PSF. (**a**) Array configuration. (**b**) PSF.

5.1.2. Imaging

To validate the performance of the presented configuration, a model based on a 1951 USAF MIL-STD-150A resolution test chart was used as the OUT. This type of geometry consists of several groups of bars (in this specific case modeled as metal plates) separated by a certain distance and is widely used to analyze and validate imaging systems. The CAD model used in the following simulation is shown in Figure 7a, and Table 1 specifies its geometry.

To perform the experiment, the OUT was placed at a standoff distance of 3 m. As can be seen in Figure 7b, the reconstruction replicates all the details of the original image. This shows that the system has a very high resolution, since it is able to reconstruct all the elements of the two groups of bars, which indicates that it is able to detect targets with an accuracy of less than 1 mm.

Table 1. Custom 1951 USAF MIL-STD-150A model geometry definition.

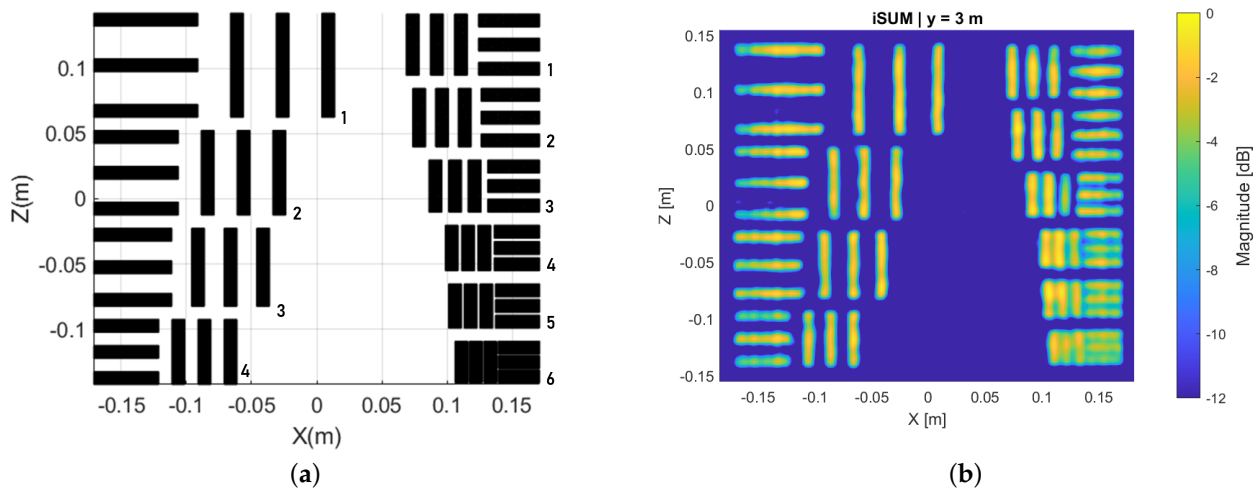| Resolution (rr) Analysis		
Distance between Bars		
	Group Number	
Element	−2	−1
1	2.5 cm	0.85 cm
2	1.75 cm	0.75 cm
3	1.5 cm	0.5 cm
4	1 cm	0.25 cm
5		0.2 cm
6		0.1 cm
Vertical spacing between elements		1 cm
Bar width (bw)		1 cm
Bar length (bl)		$3bw + 2rr$

Figure 7. XZ-plane reconstruction of the USAF-based target located 3 m from the antenna array. (**a**) CAD model. (**b**) XZ-plane reconstruction.

Runtime Simulation Performance

For imaging purposes, an XZ plane measuring 36.5 cm by 31 cm was defined, with a fine 2.5 mm discretization, resulting in a total of 18.375 pixels in the image plane. As detailed in Section 2.2, each tx_m–rx_n pair generates an individual image, leading to a substantial total of 3.136 different images to be combined within this architecture.

Remarkably, HW-1 processes these images in a mere 0.03 s, but with the utilization of HW-2 this processing time is dramatically reduced to an impressive 0.008 s. Such exceptional performance gains can be attributed to harnessing GPU resources and leveraging MATLAB's robust vector computing capabilities. Our unwavering commitment to efficiency and rapid processing drives us to continually improve our software. We actively explore alternative approaches to optimize performance, consistently pushing the boundaries of what can be achieved in the field.

6. Conclusions

This study presents a novel method to improve 2D sparse arrays, enhancing imaging performance by integrating advanced electromagnetic simulations and powerful mathematical optimization algorithms, including GAs. The results show the potential to achieve superior reconstruction quality while using less than 2% of the elements typically required by conventional full-density 2D arrays. To give context, the present version utilizes only 113 elements in contrast to the one million element requirement for a full-dense array that adheres to Nyquist's theorem, which mandates minimum separation of λ_{min} between elements. Refer to [13] for a detailed analysis of multistatic radar configurations for human body imaging. This study compares a multistatic sparse setup to established millimeter-wave imaging systems used for security screening. It should be noted that the comparison was carried out at lower frequency ranges than the ones in our study. However, the findings are still applicable to confirm that our approach is one of the most effective solutions.

The implications of this innovative method extend beyond the laboratory, with applications in On-The-Move (OTM) imaging systems that enable real-time 3D imaging of dynamic targets. Notably, the reduction in the number of elements, coupled with optimized simulation codes that leverage vector computations in MATLAB and harness the capabilities of GPUs and parallelization resources, drastically shortens simulation execution times, making the approach highly efficient.

In essence, this study is a significant advancement in imaging technology, leading to the development of highly efficient and agile imaging systems with unmatched image quality. It not only contributes substantially to the field of image processing but also lays a solid foundation for prospective advancements in the domain. This breakthrough has

far-reaching implications, including enhancing medical imaging, where the reduction in hardware requirements can lead to more accessible and cost-effective diagnostic tools. Furthermore, it can improve surveillance systems, allowing for the deployment of smaller, more discreet arrays without compromising performance, thus bolstering security and tracking capabilities. In the realm of aerospace and autonomous vehicles, this innovation can lead to more compact and lightweight radar systems, enhancing navigation and obstacle avoidance. Its manifold applications make it a revolutionary development across multiple industries, offering increased efficiency, lowered costs, and superior image quality.

Author Contributions: Conceptualization: M.A., B.G.-V., O.R., A.P., J.G. and L.P.-E.; Methodology: M.A., B.G.-V. and J.G.; Software: M.A., L.P.-E., B.G.-V. and Y.R.-V.; Validation: M.A. and B.G.-V.; Formal analysis: M.A., B.G.-V. and L.P.-E.; Investigation: M.A., B.G.-V., L.P.-E., I.S.-M. and J.G.; Resources: M.A., B.G.-V., L.P.-E. and I.S.-M.; Data curation: L.P.-E. and M.A.; Writing—original draft preparation: L.P.-E.; Writing—review and editing: M.A., B.G.-V., L.P.-E., Y.R.-V., O.R., A.P., J.G. and I.S.-M.; Visualization: M.A., B.G.-V., L.P.-E., Y.R.-V., O.R., A.P., J.G. and I.S.-M.; Supervision: M.A. and B.G.-V.; Project administration: M.A. and B.G.-V.; Funding acquisition: M.A., B.G.-V., O.R., A.P. and J.G. All authors have read and agreed to the published version of the manuscript.

Data Availability Statement: Data are contained within the article.

Conflicts of Interest: The authors declare no conflict of interest.

References

1. Ahmed, S.S. Personnel screening with advanced multistatic imaging technology. Passive and Active Millimeter-Wave Imaging XVI. In *SPIE Defense, Security, and Sensing, International Society for Optics and Photonics*; SPIE: Bellingham, WA, USA, 2013; p. 87150B.
2. Siegel, P.H. Terahertz technology. *IEEE Trans. Microw. Theory Tech.* **2002**, *50*, 910–928 [CrossRef]
3. Sheen, D.; McMakin, D.; Hall, T. Three-dimensional millimeter-wave imaging for concealed weapon detection. *IEEE Trans. Microw. Theory Tech.* **2001**, *49*, 1581–1592. [CrossRef]
4. Sheen, D.M.; Hall, T.E.; Severtsen, R.H.; McMakin, D.L.; Hatchell, B.K.; Valdez, P.L.J. Active wideband 350 GHz imaging system for concealed-weapon detection. In *Society of Photo-Optical Instrumentation Engineers (SPIE) Conference Series*; SPIE: Bellingham, WA, USA, 2009; Volume 7309. [CrossRef]
5. Sheen, D.; McMakin, D.; Hall, T.; Severtsen, R. Active millimeter-wave standoff and portal imaging techniques for personnel screening. In Proceedings of the IEEE Conference on Technologies for Homeland Security, HST '09, Waltham, MA, USA, 11–12 May 2009; pp. 440–447. [CrossRef]
6. Friederich, F.; Von Spiegel, W.; Bauer, M.; Meng, F.; Thomson, M.D.; Boppel, S.; Lisauskas, A.; Hils, B.; Krozer, V.; Keil, A.; et al. THz active imaging systems with real-time capabilities. *IEEE Trans. Terahertz Sci. Technol.* **2011**, *1*, 183–200. [CrossRef]
7. Cooper, K.; Dengler, R.; Llombart, N.; Thomas, B.; Chattopadhyay, G.; Siegel, P. THz Imaging Radar for Standoff Personnel Screening. *IEEE Trans. Terahertz Sci. Technol.* **2011**, *1*, 169–182. [CrossRef]
8. Soumekh, M. Bistatic synthetic aperture radar inversion with application in dynamic object imaging. *IEEE Trans. Signal Process.* **1991**, *39*, 2044–2055. [CrossRef] [PubMed]
9. Grajal, J.; Badolato, A.; Rubio-Cidre, G.; Úbeda Medina, L.; Mencia-Oliva, B.; Garcia-Pino, A.; Gonzalez-Valdes, B.; Rubiños, O. 3-D High-Resolution Imaging Radar at 300 GHz With Enhanced FoV. *IEEE Trans. Microw. Theory Tech.* **2015**, *63*, 1097–1107. [CrossRef]
10. Burkholder, R.; Gupta, I.; Johnson, J. Comparison of monostatic and bistatic radar images. *IEEE Antennas Propag. Mag.* **2003**, *45*, 41–50. [CrossRef]
11. Yates, G.; Horne, A.; Blake, A.; Middleton, R. Bistatic SAR image formation. *IEE-Proc.-Radar, Sonar Navig.* **2006**, *153*, 208–213. [CrossRef]
12. Zhuge, X.; Yarovoy, A.G. A Sparse Aperture MIMO-SAR-Based UWB Imaging System for Concealed Weapon Detection. *IEEE Trans. Geosci. Remote. Sens.* **2011**, *49*, 509–518. [CrossRef]
13. Gonzalez-Valdes, B.; Alvarez, Y.; Mantzavinos, S.; Rappaport, C.M.; Las-Heras, F.; Martinez-Lorenzo, J.A. Improving Security Screening: A Comparison of Multistatic Radar Configurations for Human Body Imaging. *IEEE Antennas Propag. Mag.* **2016**, *58*, 35–47. [CrossRef]

14. Ahmed, S.S.; Genghammer, A.; Schiessl, A.; Schmidt, L.-P. Fully electronic active E-band personnel imager with 2 m2 aperture. In Proceedings of the 2012 IEEE/MTT-S International Microwave Symposium Digest, Montreal, QC, Canada, 17–22 June 2012; pp. 1–3. [CrossRef]

15. Ahmed, S.S.; Schiessl, A.; Schmidt, L.-P. A Novel Fully Electronic Active Real-Time Imager Based on a Planar Multistatic Sparse Array. *IEEE Trans. Microw. Theory Tech.* **2011**, *59*, 3567–3576. [CrossRef]

16. Ahmed, S.S.; Schiess, A.; Schmidt, L.-P. Near field mm-wave imaging with multistatic sparse 2D-arrays. In Proceedings of the 2009 European Radar Conference (EuRAD), Rome, Italy, 30 September–2 October 2009; pp. 180–183.

17. Rigling, B.D.; Moses, R.L. Three-dimensional surface reconstruction from multistatic SAR images. *IEEE Trans. Image Process.* **2005**, *14*, 1159–1171. [CrossRef] [PubMed]

18. Detlefsen, J. Application of Multistatic Radar Principles to Short-Range Imaging. *Iee Proc. Commun. Radar Signal Process.* **1986**, *133*, 658–663 [CrossRef]

19. Stojanovic, I.; Çetin, M.; Karl, W.C. Sensing of Monostatic and Multistatic SAR. *IEEE Geosci. Remote. Sens. Lett.* **2013**, *10*, 1444–1448. [CrossRef]

20. Guido, R.C.; Pedroso, F.; Contreras, R.C.; Rodrigues, L.C.; Guariglia, E.; Neto, J.S. Introducing the Discrete Path Transform (DPT) and its applications in signal analysis, artefact removal, and spoken word recognition. *Digit. Signal Process.* **2021**, *117*, 103158. [CrossRef]

21. Guariglia, E.; Silvestrov, S. Fractional-Wavelet Analysis of Positive definite Distributions and Wavelets on D'(C). In *Engineering Mathematics II*; Silvestrov, S., Ed.; Springer International Publishing: Cham, Switzerland, 2016; pp. 337–353.

22. Yang, L.; Su, H.; Zhong, C.; Meng, Z.; Luo, H.; Li, X.; Tang, Y.Y.; Lu, Y. Hyperspectral image classification using wavelet transform-based smooth ordering. *Int. J. Wavelets, Multiresolution Inf. Process.* **2019**, *17*, 1950050. [CrossRef]

23. Guariglia, E. Harmonic Sierpinski Gasket and Applications. *Entropy* **2018**, *20*, 714. [CrossRef]

24. Zheng, X.; Tang, Y.Y.; Zhou, J. A Framework of Adaptive Multiscale Wavelet Decomposition for Signals on Undirected Graphs. *IEEE Trans. Signal Process.* **2019**, *67*, 1696–1711. [CrossRef]

25. Guariglia, E. Primality, Fractality, and Image Analysis. *Entropy* **2019**, *21*, 304 [CrossRef]

26. Berry, M.V.; Lewis, Z.V.; Nye, J.F. On the Weierstrass-Mandelbrot fractal function. *Proc. R. Soc. Lond. Math. Phys. Sci.* **1980**, *370*, 459–484. [CrossRef]

27. Molaei, A.M.; Hu, S.; Skouroliakou, V.; Fusco, V.; Chen, X.; Yurduseven, O. Fourier Compatible Near-Field Multiple-Input Multiple-Output Terahertz Imaging With Sparse Non-Uniform Apertures. *IEEE Access* **2021**, *9*, 157278–157294. [CrossRef]

28. Ahi, K. Mathematical Modeling of THz Point Spread Function and Simulation of THz Imaging Systems. *IEEE Trans. Terahertz Sci. Technol.* **2017**, *7*, 747–754. [CrossRef]

29. Shami, T.M.; El-Saleh, A.A.; Alswaitti, M.; Al-Tashi, Q.; Summakieh, M.A.; Mirjalili, S. Particle Swarm Optimization: A Comprehensive Survey. *IEEE Access* **2022**, *10*, 10031–10061. [CrossRef]

30. Shi, Y.; Eberhart, R.C. Empirical study of particle swarm optimization. In Proceedings of the Congress on Evolutionary Computation CEC 99, Washington, DC, USA, 6–9 July 1999; Volume 3, pp. 1945–1949. [CrossRef]

31. Kirkpatrick, S.; Gelatt, J.; Vecci, M. Optimization by simulated annealing. *Science* **1983**, *220*, 671–680. [CrossRef]

32. Hajek, B. A tutorial survey of theory and applications of simulated annealing. In Proceedings of the 1985 24th IEEE Conference on Decision and Control, Fort Lauderdale, FL, USA, 11–13 December 1985; pp. 755–760. [CrossRef]

33. Altbawi, S.M.A.; Khalid, S.B.A.; Mokhtar, A.S.B.; Shareef, H.; Husain, N.; Yahya, A.; Haider, S.A.; Moin, L.; Alsisi, R.H. An Improved Gradient-Based Optimization Algorithm for Solving Complex Optimization Problems. *Processes* **2023**, *11*, 498. [CrossRef]

34. Malu, M.; Dasarathy, G.; Spanias, A. Bayesian Optimization in High-Dimensional Spaces: A Brief Survey. In Proceedings of the 2021 12th International Conference on Information, Intelligence, Systems and Applications (IISA), Chania Crete, Greece, 12–14 July 2021; pp. 1–8. [CrossRef]

35. Grana-Varela, M.; Arias, M.; Rubinos, O.; Garcia-Pino, A. Rapid dual reflector shaping using Ant Colony Optimization, fast iterated PO and asymptotic MFIE. In Proceedings of the 2009 3rd European Conference on Antennas and Propagation, Berlin, Germany, 23–27 March 2009; pp. 2731–2735.

36. Bergmann, J.R.; Hasselmann, F.J.; Teixeira, F.L.; Rego, C.G. A Comparison between Techniques for Global Surface Interpolation in Shaped Reflector Analysis. *IEEE Trans. Antennas Propag.* **1994**, *42*, 47–53. [CrossRef]

37. Holland, J.H. *Adaptation in Natural and Artificial Systems*, 2nd ed.; University of Michigan Press: Ann Arbor, MI, USA, 1992.

38. Beasley, D.; Bull, D.R.; Martin, R.R. An Overview of Genetic Algorithms: Part 1, Fundamentals. *Univ. Comput.* **1993**, *15*, 58–69.

39. Srinivas, M.; Patnaik, L. Genetic algorithms: A survey. *Computer* **1994**, *27*, 17–26. [CrossRef]

40. Ares-Pena, F.; Rodriguez-Gonzalez, J.; Villanueva-Lopez, E.; Rengarajan, S. Genetic algorithms in the design and optimization of antenna array patterns. *IEEE Trans. Antennas Propag.* **1999**, *47*, 506–510. [CrossRef]

41. Perez-Eijo, L.; Gonzalez-Valdes, B.; Arias, M.; Tilves, D.; Rodriguez-Vaqueiro, Y.; Rubiños-López, O.; Pino, A.; García-Rial, F.; Grajal, J. A Physical Optics Simulator for Multireflector THz Imaging Systems. *IEEE Trans. Terahertz Sci. Technol.* **2019**, *9*, 476–483. [CrossRef]

42. Wehner, D.R. *High-Resolution Radar*, 2nd ed.; Artech House: London, UK, 1995.

43. Teer, T.; Goodman, N. Multistatic SAR algorithm with image combination. In Proceedings of the 2006 IEEE Conference on Radar, Verona, NY, USA, 24–27 April 2006; p. 8. [CrossRef]

44. Ahmed, S.S.; Schiessl, A.; Gumbmann, F.; Tiebout, M.; Methfessel, S.; Schmidt, L. Advanced microwave imaging. *IEEE Microw. Mag.* **2012**, *13*, 26–43. [CrossRef]